

Fe–Mo and Co–Mo Catalysts with Varying Composition for Multi-Walled Carbon Nanotube Growth

Mariya A. Kazakova,* Vladimir L. Kuznetsov, Sofia N. Bokova-Sirosh, Dmitry V. Krasnikov, Georgiy V. Golubtsov, Anatoliy I. Romanenko, Igor P. Prosvirin, Arcadiy V. Ishchenko, Andrey S. Orekhov, Andrey L. Chuvilin, and Elena D. Obraztsova

The formation of active component of Fe–Mo and Co–Mo catalysts for carbon nanotube growth with variable Mo content is studied with in situ XRD, XPS, and STEM&EDX. The activation of bimetallic Fe–Mo catalysts under the growth conditions leads to the formation of Fe–Mo alloy particles in contrast to Co-containing catalysts in which active alloy incorporates only a small portion of Mo (<2–3 at.%). The stable carbide formation for these systems is not detected. The effect of Mo content in Fe–Mo and Co–Mo catalysts on the properties of MWCNTs is additionally investigated using the Raman spectroscopy in combination with measurements of the temperature dependence of conductivity. It is shown that MWCNT defectiveness depends on the active component composition for both Fe–Mo and Co–Mo catalysts. The current carrier concentration for the MWCNTs grown on Fe–Mo catalysts slightly increases with the Mo content. The opposite effect is observed for the tubes grown on Co–Mo catalysts, showing a decrease in the current carrier concentration with the increase of Mo concentration.

electromagnetic radiation over a wide range of wavelengths, etc. CNTs are considered as promising candidates for many potential applications such as nanocomposite materials, catalyst and catalyst supports, field emitters, sensors, energy storage devices, hydrogen storage, fuel cells, nanoelectronics, bionanomaterials, and nanomedicine.^[1–18] Generally, most of multi-walled carbon nanotubes (MWCNTs) are used to improve the physical and chemical characteristics of numerous composite materials based on polymeric, metal and oxide matrices.^[19–27] Nowadays, the most common approach of the nanotube synthesis in a large-scale is the catalytic chemical vapor deposition (CCVD).^[28,29] However, production of high-purity MWCNTs with adjusted properties and low cost remains challenging, despite of the fact that their world consumption is more than 3000 tons per year.^[30] The CCVD method leads to the production of MWCNTs with a sufficiently high number of microstructural defects, as well as catalyst and amorphous carbon impurities. High defectiveness of tube walls leads to deterioration of their properties including mechanical strength, electrical and thermal conductivity. Moreover, the lack of growth control leads to the production of nanotubes with a wide range of diameters.

1. Introduction

Carbon nanotubes (CNTs) are among the key nanostructures that have been actively developed and investigated during the last two decades due to their unique electrophysical properties, such as high electrical and thermal conductivity, high mechanical strength, relative chemical inertness, the ability to absorb

Dr. M. A. Kazakova, Dr. V. L. Kuznetsov, Dr. D. V. Krasnikov, G. V. Golubtsov, Dr. I. P. Prosvirin, Dr. A. V. Ishchenko
Novosibirsk State University
Pirogova st. 2, 630090 Novosibirsk, Russia
E-mail: mas@catalysis.ru

Dr. M. A. Kazakova, Dr. V. L. Kuznetsov, Dr. D. V. Krasnikov, G. V. Golubtsov, Dr. I. P. Prosvirin, Dr. A. V. Ishchenko
Boreskov Institute of Catalysis SB RAS
pr. Lavrentieva 5, 630090 Novosibirsk, Russia

Dr. S. N. Bokova-Sirosh, Dr. E. D. Obraztsova
A.M. Prokhorov General Physics Institute RAS
Vavilov st. 38, 119991 Moscow, Russia

Dr. S. N. Bokova-Sirosh, Dr. E. D. Obraztsova
National Research Nuclear University MEPhI
Kashirskoye shosse 31, 115409 Moscow, Russia

Prof. A. I. Romanenko
Nikolaev Institute of Inorganic Chemistry SB RAS
Lavrentieva ave. 3, 630090 Novosibirsk, Russia

Dr. A. S. Orekhov
A.V. Shubnikov Institute of Crystallography RAS
Leninskii pr. 59, 119333 Moscow, Russia

Dr. A. S. Orekhov
National Research Center “Kurchatov Institute”
pl. Kurchatova 1, 123182 Moscow, Russia

Dr. A. L. Chuvilin
CIC nanoGUNE
Tolosa Hiribidea, 76, E-20018 Donostia – San Sebastian, Spain

Dr. A. L. Chuvilin
IKERBASQUE
Basque Foundation for Science
E-48013 Bilbao, Spain

 The ORCID identification number(s) for the author(s) of this article can be found under <https://doi.org/10.1002/pssb.201700260>.

DOI: 10.1002/pssb.201700260

It is known that the properties of MWCNTs are primarily determined by the composition of catalyst and support, size of the catalytic particles, catalyst activation conditions, composition of the hydrocarbon feedstock, and other synthesis parameters like temperature, gas delivery rate, reactor design, etc.^[31,32] At the same time, the most important role is played by the composition and structure of catalysts which determine the morphology and microstructure of the nanotubes grown over their surface. Metals, such as iron, cobalt, and nickel, and their compositions are commonly used as catalysts for the synthesis of MWCNTs.^[33–36] It is known that the addition of a promoter to the catalyst can enhance the yield of nanotubes and affect their morphology. Metals, such as Mn, Mo, Cu, Pd, W, V, etc. were suggested as the catalyst promoters as described here.^[37–39] Molybdenum is widely used as an effective promoter for the catalysts based on iron group metals (Fe, Co, Ni) for CNTs formation in the CCVD reaction.^[40–45] However, studies on the formation of Fe–Mo and Co–Mo active components and a detailed investigation of the Mo promotion role during the CNT nucleation have not been disclosed yet.

This work aims to investigate the formation and activation of Fe–Mo and Co–Mo catalysts obtained by the Pechini method for the synthesis of MWCNTs directly under the reaction conditions. The main focus is to evaluate the effects of the catalyst composition along with the active metal ratio (Fe–Mo, Co–Mo) on the formation of MWCNTs and their structural characteristics.

2. Experimental and Methodology

MWCNTs were grown using catalysts with a variable composition of Fe–Mo and Co–Mo active components. The bicomponent catalysts containing 30–70 wt.% of Fe–Mo and Co–Mo as the active component with a variable ratio of active metals (Fe/Mo and Co/Mo = 2:1–29:1) and Al-containing oxides as a support were prepared with the Pechini-type method.^[46–48] This method is based on the preliminary distribution of metal ions (Fe or Co, Mo and Al) in a three-dimensional polymeric matrix comprising citric acid and ethylene glycol. The subsequent calcination of this matrix at 560 °C leads to the formation of a system of mixed spinel-like oxides.

Two sets of MWCNTs with different average diameters were obtained by catalytic decomposition of ethylene over Fe–Mo and Co–Mo catalysts with different compositions in a quartz tubular reactor at 670 °C. The as-prepared catalysts were brought to constant weight and stored without access of air in order to prevent the water adsorption. To grow carbon nanotubes, the catalyst powder (50 mg) was placed into the reactor preheated up to the required temperature in an Ar flow. After 10 min of purging with Ar, the catalyst was exposed to a flow of ethylene–argon mixture (C₂H₄/Ar = 1:1, flow 400 sccm) for 15 min. Active metal particles were generated in situ on the surface of the oxide matrix during catalyst reduction by ethylene. The MWCNTs formation was controlled by the product yield. The yield of MWCNTs after the ethylene catalytic decomposition on the surface of Co–Mo and Fe–Mo was calculated using the formula below:

MWCNT yield =

$$\frac{(\text{weight of MWCNT deposited}) - (\text{weight of catalyst used})}{\text{weight of catalyst used}}$$

The relative error of MWCNT yield measurements was $\pm 5\%$. The MWCNT morphology and diameter distribution were characterized by High-Resolution Transmission Electron Microscopy (HRTEM), Scanning Transmission Electron Microscopy (STEM), and X-ray Energy Dispersion Spectroscopy (EDS). The TEM measurements were carried out on a FEI Titan 60-300 TEM/STEM electron microscope equipped with x-FEG electron source, monochromator and Cs-spherical aberration corrector, and operating at 80 kV accelerating voltage. Nanotube diameter distributions were estimated with an electron microscope JEM-2010 using 300-400 MWCNT images obtained by TEM at magnifications of $\times 50\,000$ and $\times 400\,000$. The specific surface area (SBET) of the catalysts and MWCNTs produced was determined by thermal desorption of argon with a SORBI-M instrument (ZAO Meta, Russia).

X-ray diffraction (XRD) measurements were performed at Siberian Synchrotron and Terahertz Radiation Center of the Budker Institute of Nuclear Physics. In situ XRD measurements at 20–700 °C were carried out inside a XRK-900 reactor chamber (Anton Paar, Austria) equipped with a fast, parallax-free one-coordinate X-ray detector OD-3M. XRD data on the size of oxide particles of the initial catalytic systems and metal particles of catalysts after different activation procedures were obtained from analysis of the peak width, increased in comparison with the standard (SRM676) of the corresponding XRD lines, and from evaluation of the size of coherent scattering region.

Photoelectron spectra were recorded using a SPECS spectrometer with a PHOIBOS-150-MCD-9 hemispherical energy analyzer (Al K_α, irradiation, $h\nu = 1486.6$ eV, 200 W). The samples were supported onto double-sided conducting copper scotch tape. The binding energy (BE) scale was preliminarily calibrated by the position of the peaks of Au4f_{7/2} (BE = 84.0 eV) and Cu2p_{3/2} (BE = 932.67 eV) core levels. The binding energy of peaks was calibrated by the position of the C1s peak (BE = 285.0 eV) corresponding to the surface hydrocarbon-like deposits (C–C and C–H bonds). Survey spectra and the narrow spectral regions (Al2p, Mo3d, C1s, O1s, Fe2p, and Co2p) were recorded at the analyzer pass energy of 20 eV. Spectral analysis and data processing were performed with XPS Peak 4.1 program.^[49] The relative content of the elements on the catalyst surfaces and the atomic ratios of their concentrations were calculated from the integral intensities of photoelectron lines corrected with respect to the corresponding atomic sensitivity factors.^[50]

The Raman spectroscopic analysis of MWCNT powders was performed with a Renishaw's in Via Reflex spectrometer in microscopic configuration with the spectral resolution of 2 cm^{-1} . The radiation of Ar laser with the wavelength of 514.5 nm was used for spectrum excitation. The Raman spectra of MWCNTs were recorded in three spectral regions: D (disorder-induced), G (graphite), and 2D (two-phonon scattering) bands. All the spectra were normalized with respect to D-mode.

The temperature dependences of conductivity $\sigma(T)$ of MWCNTs produced with different types of catalysts were measured by a four point-probe technique in the temperature range from 4.2 to 300 K. The electrical contacts were made by 0.1 mm silver wires. For electrical measurements, the MWCNT powder was pressed in a glass cylinder. Our previous studies of powder carbon nanostructures carried out by this method^[51, 52] showed that the results of conductivity measurements are stable and reproducible.

3. Results and Discussion

3.1. Investigation of Catalyst Activation and CNT Nucleation on Co–Mo and Fe–Mo Nanoparticles by In Situ XRD and XPS

The results of in situ XRD experiments on high temperature treatment of mono-component iron and cobalt catalysts with a C_2H_4 –Ar mixture were described previously.^[53] For the mono-component Fe catalyst, the formation of iron carbides was observed under the reaction conditions. In the case of monocomponent Co catalysts, treatment with the C_2H_4 –Ar mixture resulted in the formation of fcc metal Co particles containing dissolved carbon without subsequent carbide formation. In this work, we investigated the in situ activation of multicomponent Fe–Mo and Co–Mo catalysts during MWCNTs growth.

Figures 1 and 2 display XRD patterns of the 40%(Fe₂Mo)/Al₂O₃ and 40%(Co₂Mo)/Al₂O₃ samples evolution at the reaction temperature (670 °C) during ethylene treatment. The presence of finely dispersed mixed-type spinel structures based on Fe and Al was obvious for the initial 40%(Fe₂Mo)/Al₂O₃ sample (Figure 1). However, when the sample is heated to 550 °C, a slight structuring of these phases is observed. Reflexes relating to the molybdenum oxide phase are not detected, which can be

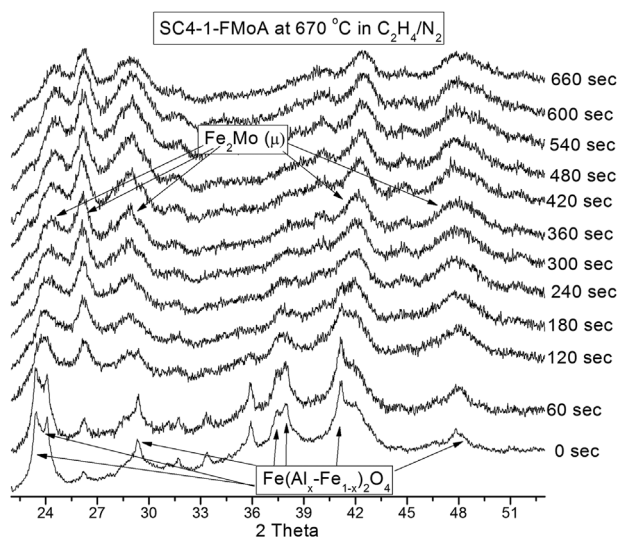


Figure 1. Time resolved in situ XRD patterns of the 40%(Fe₂Mo)/Al₂O₃ catalyst evolution at the reaction temperature (670 °C) during ethylene treatment.

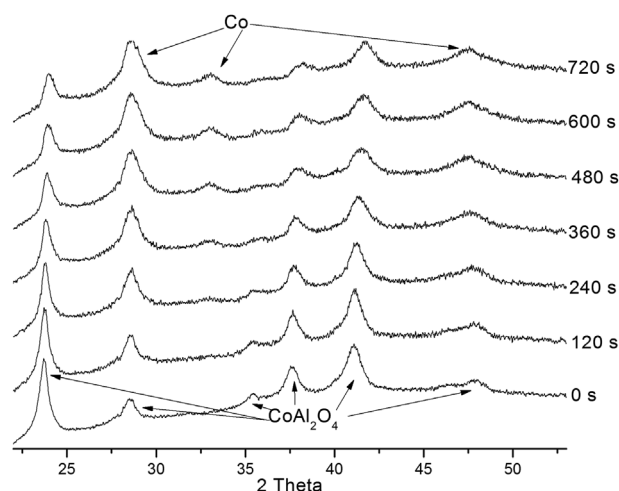


Figure 2. Time resolved in situ XRD patterns of the 40%(Co₂Mo)/Al₂O₃ catalyst evolution at the reaction temperature (670 °C) during ethylene treatment.

explained by the high dispersion of this phase. After the introduction of ethylene, the spinel phases are reduced with the formation of the Fe₂Mo intermetallide and the μ phase, which has a lattice similar to the intermetallide and is enriched with molybdenum in the range of 40–45%. These observations correlate with the STEM data on the formation of Fe–Mo alloy particles (Figure 8A).

In the case of the initial 40%(Co₂Mo)/Al₂O₃ sample, a set of reflexes corresponding to the CoAl₂O₄ phase is observed (Figure 2). There are no reflexes associated with molybdenum oxide, which can be explained by the high dispersion of these phases.

When the sample is heated, no phase transformations occur, however, the slight shift of the reflexes becomes visible. A preliminary reduction of the metal particles is not confirmed. The further supply of ethylene results in a partial reduction of the sample with the formation of metal particles having a fcc lattice (pure cobalt or a solid solution of cobalt and molybdenum with a Mo content of a couple of percent). This phase most likely can be suggested as an active component. Intermetallic and Co₃Mo and μ -phases, whose presence could be expected from the phase diagram and catalyst composition, are not observed. This phenomenon can be explained by the overall high dispersion of the system.

The results of the in situ XRD experiment for the Co–Mo and Fe–Mo samples with the metal ratio Co(Fe)/Mo = 16:1 are shown in Figures 3 and 4.

The 40%(Co₁₆Mo)/Al₂O₃ and 40%(Fe₁₆Mo)/Al₂O₃ samples are characterized by a higher activity in the MWCNTs growth reaction in comparison with the 40%(Fe(Co)₂Mo)/Al₂O₃ samples (Tables 1 and 2). This significantly decreases the effective operation time for in situ XRD experiment due to the deposition of a bulky nanotube layer.

Taking into account the high dispersion of the samples, the possibility to obtain more detailed information is limited. According to the phase diagram and experimental data, in the case of the 40%(Co₁₆Mo)/Al₂O₃ sample one may propose the

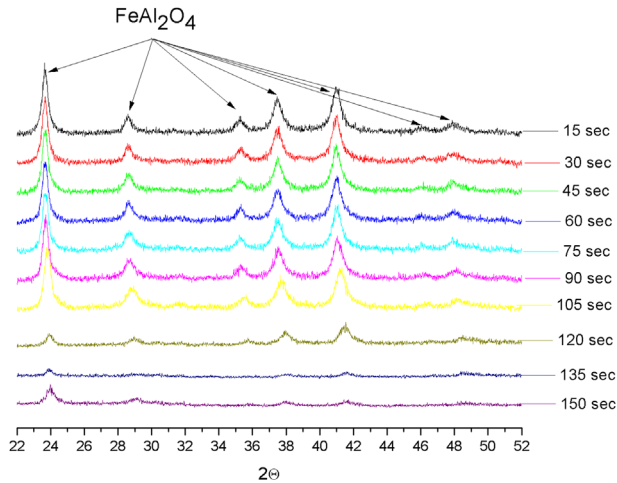


Figure 3. Time resolved in situ XRD patterns of the 40%(Fe₁₆Mo)/Al₂O₃ catalyst evolution at the reaction temperature (670 °C) during ethylene treatment.

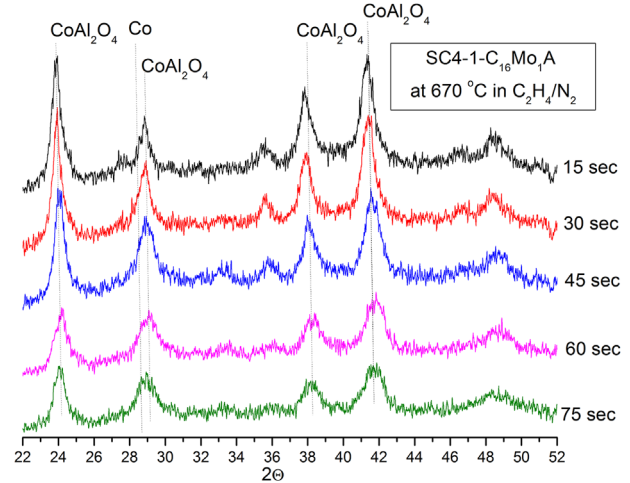


Figure 4. Time resolved in situ XRD patterns of the 40%(Co–Mo)/Al₂O₃ catalyst with the metal ratio Co/Mo = 16:1 evolution at the reaction temperature (670 °C) during ethylene treatment.

formation of the fcc phase of cobalt particles or the phase of cobalt diluted with molybdenum up to a couple of percent. The formation of other metallic phases does not occur. In the case of the 40%(Fe₁₆Mo)/Al₂O₃ catalyst, Fe–Mo containing phases are not detected because of the fast dispersion of active species in

carbon deposits. At a temperature of 550–600 °C, only the catalyst sintering is observed for 40%(Fe₁₆Mo)/Al₂O₃.

The XPS method was used to obtain more detailed information about the state of active component of Co–Mo and Fe–Mo catalysts during the carbon nanotube nucleation

Table 1. Properties of Fe–Mo catalysts and produced MWCNTs.

Catalysts wt.% (Fe _x Mo)/Al ₂ O ₃	Fe/Mo molar ratio	S _{BET} of catalysts, m ² g ⁻¹	Yield of MWCNTs, g _{MWCNT} /g _{cat}	S _{BET} of MWCNTs, m ² g ⁻¹	d _{MWCNT} , nm	I _{2D} /I _D	I _D /I _G
40% (Fe ₂ Mo)/Al ₂ O ₃	2:1	146.9	7.7	363	8.4	0.43	0.78
40% (Fe ₄ Mo)/Al ₂ O ₃	4:1	168.1	17.2	349	–	0.42	1.01
40% (Fe ₈ Mo)/Al ₂ O ₃	8:1	168.9	21.8	322	9.3	0.43	1.09
40% (Fe ₁₆ Mo)/Al ₂ O ₃	16:1	183.3	22.0	376	9.8	0.41	1.17
40% (Fe ₂₉ Mo)/Al ₂ O ₃	29:1	168.5	21.8	297	–	0.47	1.20
40% Fe/Al ₂ O ₃	–	169.1	16.9	319	11.9	0.55	1.25
50% (Fe ₁₆ Mo)/Al ₂ O ₃	16:1	242.1	20.4	266	10.1	0.47	0.99
60% (Fe ₁₆ Mo)/Al ₂ O ₃	16:1	155.3	16.9	304	8.6	0.46	0.97
70% (Fe ₁₆ Mo)/Al ₂ O ₃	16:1	119.4	18.0	302	9.4	0.45	0.98

Table 2. Properties of Co–Mo catalysts and produced MWCNTs.

Catalysts wt.% (Co _x Mo)/Al ₂ O ₃	Co/Mo molar ratio	S _{BET} of catalysts, m ² g ⁻¹	Yield of MWCNT, g _{MWCNT} /g _{cat}	S _{BET} of MWCNTs, m ² g ⁻¹	d _{MWCNT} , nm	I _{2D} /I _D	I _D /I _G
40% (Co ₂ Mo)/Al ₂ O ₃	2:1	68.7	3.0	195	10.7	0.56	0.78
40% (Co ₄ Mo)/Al ₂ O ₃	4:1	189.7	11.0	289	9.4	0.37	1.01
40% (Co ₈ Mo)/Al ₂ O ₃	8:1	113.9	18.7	332	–	0.29	1.09
40% (Co ₁₆ Mo)/Al ₂ O ₃	16:1	129.6	23.0	377	8.5	0.26	1.17
40% (Co ₂₉ Mo)/Al ₂ O ₃	29:1	118.7	22.3	360	–	0.27	1.20
40% Co/Al ₂ O ₃	–	136.3	23.5	382	7.5	0.24	1.25
30% (Co ₁₆ Mo)/Al ₂ O ₃	16:1	115.1	9.8	392	8.6	0.23	1.07
50% (Co ₁₆ Mo)/Al ₂ O ₃	16:1	160.9	20.0	307	9.0	0.33	1.12
60% (Co ₁₆ Mo)/Al ₂ O ₃	16:1	140.7	19.2	287	9.2	0.36	1.11

process. For both initial catalysts: 40%(Co₁₆Mo)/Al₂O₃ and 40%(Co₂Mo)/Al₂O₃, it was found that cobalt and molybdenum present in the Co²⁺ and Mo⁶⁺ states. In this case, the cobalt line for the initial catalyst is almost identical to the corresponding signal of the model spinel CoAl₂O₄, which coincides with the XRD data (Figure 4).

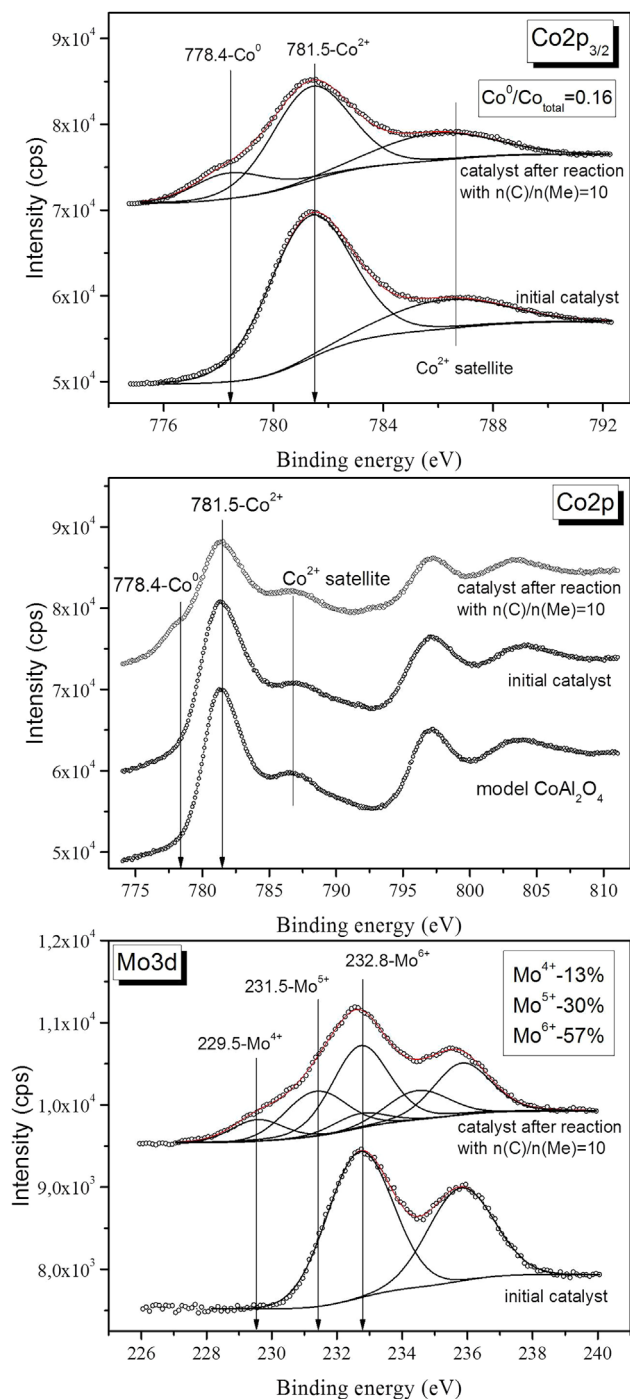


Figure 5. Co_{2p_{3/2}}, Co_{2p}, and Mo_{3d} XPS spectra for the initial 40%(Co₁₆Mo)/Al₂O₃ sample and after treatment with the reaction medium (C₂H₄/Ar = 1:4, flow 400 sccm).

After the treatment under the reaction conditions (C₂H₄/Ar = 1:4, flow 400 sccm during 20 s), that correspond to the introduction of 10 carbon atoms per atom of Co(Mo), about 16% of cobalt is reduced to Co⁰. The formation of metallic molybdenum during exposure of the catalyst to the similar conditions is not detected. Nevertheless, there is a general tendency of Mo to reduce, as can be seen from the presence of such molybdenum species like Mo⁴⁺ and Mo⁵⁺ (Figure 5). The obtained results correlate with the EDS data (Figure 8) indicating a partial incorporation of molybdenum into the Co–Mo active component. In the case of Fe-containing catalyst, the pattern is more complex. For both catalytic systems, namely 40%(Fe₁₆Mo)/Al₂O₃ and 40%(Fe₂Mo)/Al₂O₃ sample, the lines at 711.6 and 332.8 eV corresponding to pure Fe³⁺ and Mo⁶⁺ species are observed in the XPS spectra of Fe_{2p} and Mo_{3d}. After treatment with the reaction mixture (C₂H₄/Ar = 1:4, flow 400 sccm, 20 s) that correspond to the introduction of 10 carbon atoms per Fe(Mo) atom, a stepped spectrum of Fe (Fe_{2p} line) is obtained (Figure 6).

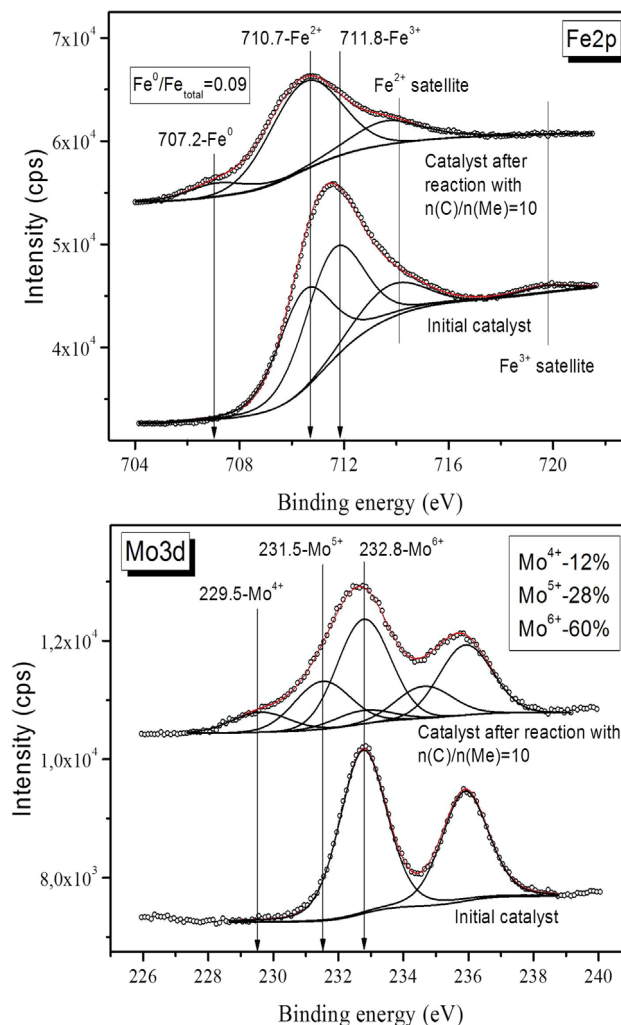


Figure 6. Fe_{2p} and Mo_{3d} XPS spectra for the initial 40%(Fe₁₆Mo)/Al₂O₃ sample and after treatment with the reaction medium (C₂H₄/Ar = 1:4, flow 400 sccm, during 20 s). C_{1s} spectra for the 40%(Fe₁₆Mo)/Al₂O₃ catalyst after the reaction.

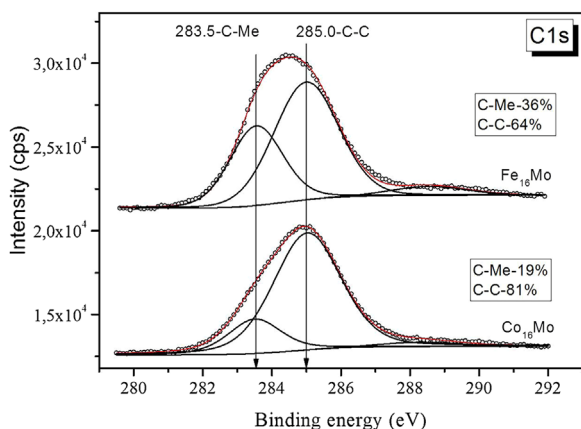


Figure 7. C1s XPS spectra for the 40%(Fe₁₆Mo)/Al₂O₃ and 40%(Co₁₆Mo)/Al₂O₃ catalysts after treatment with the reaction medium (C₂H₄/Ar = 1:4, flow 400 sccm, during 20 s).

The observed Fe³⁺ to Fe²⁺ transition is confirmed by the disappearance of the Fe³⁺ satellite in the region of 719.8 eV. At the same time, the total proportion of iron in the metallic state is near 9%. These results suggest a stepwise reduction of Fe³⁺ to Fe⁰ through Fe²⁺. Moreover, the second stage of Fe²⁺ reduction to Fe⁰ is rate-limiting. In the case of molybdenum, the pattern is similar to that observed for 40%(Co₁₆Mo)/Al₂O₃. A partial reduction of Mo⁶⁺ to Mo⁵⁺ and Mo⁴⁺ occurs. According to XPS data, the Mo⁶⁺/Mo⁵⁺/Mo⁴⁺ ratio is equal to 12:28:60. Apparently, similar picture of the molybdenum reduction is observed for the 40%(Co₁₆Mo)/Al₂O₃ and 40%(Fe₁₆Mo)/Al₂O₃ catalysts. A slight difference in the Mo⁶⁺/Mo⁵⁺/Mo⁴⁺ ratio can be explained by the error of the experiment or the influence of the hydrogen spillover from the more reduced cobalt species in comparison with the iron ones.

The analysis of the C1s XPS spectra reveals two signals with the binding energies of 285.0 and 283.5 eV, which are related to carbon bound with another carbon or metal, respectively (Figure 7). In the case of Fe-containing catalysts, the fraction of carbon bonded to the metal is almost twice as high as in the case of the Co-containing catalyst.

This fact can be explained in two ways. Firstly, the solubility of carbon in iron is much higher than in cobalt. Secondly, the reduction rate of cobalt is much higher, and the number of MWCNTs (which give the C–C contribution to the carbon line) obtained on the 40%(Co₁₆Mo)/Al₂O₃ catalyst is higher than for the 40%(Fe₁₆Mo)/Al₂O₃ catalyst.

3.2. The Effect of Catalyst Composition on the MWCNT Production and Their Structure

One of the objectives of this work was to investigate the influence of various catalyst parameters, such as the content of Co–Mo and Fe–Mo active components and the ratios of active metals (Fe/Mo and Co/Mo), on the activity in MWCNTs production and their structural characteristics. In this case, two series of Fe–Mo/Al₂O₃ and Co–Mo/Al₂O₃ catalysts were prepared: the first series includes the samples containing 40 wt.% of Fe–Mo and Co–Mo

active components with metal ratios of 2:1, 4:1, 8:1, 16:1, and 29:1; the second series includes the catalysts with different content of active components and a similar molar ratio of active metals equal to 16:1 (40–70 wt.% for Fe–Mo and 30–60 wt.% for Co–Mo). The synthesized samples are designated as x%(Co(Fe)_yMo)/Al₂O₃, where x is the content of active component (wt.%), and y is the molar ratio of metals. For instance, in the case of 40%(Fe₁₆Mo)/Al₂O₃, the content of active component is 40 wt.% and the metal ratio is Fe/Mo = 16:1. Fe and Co-based catalysts were used for comparison purposes in order to elucidate the effects of Mo addition. The chemical analysis data for the catalysts obtained by XRF method are in good agreement with the calculated data.

Data on the activity of catalysts with the variable content of active component and ratio of the active component metals (Fe/Mo and Co/Mo), the specific surface area of the catalysts and MWCNTs produced, and the average external diameters of MWCNTs (TEM data) are listed in Tables 1 and 2.

The variation in the concentration of the active component in the catalysts strongly influences the yield of MWCNTs. The lowest yield of MWCNTs is observed for the Co–Mo catalyst containing 30 wt.% of the active component (Table 2). The catalytic tests show that the highest activity among all of the Fe–Mo catalysts prepared is observed for the 40%(Fe₁₆Mo)/Al₂O₃ system (Table 1). In the case of Co-based catalysts, the greatest activity is observed for the sample containing only Co without the addition of molybdenum. Apparently, this fact can be explained in terms of different ability of Mo to form alloys with

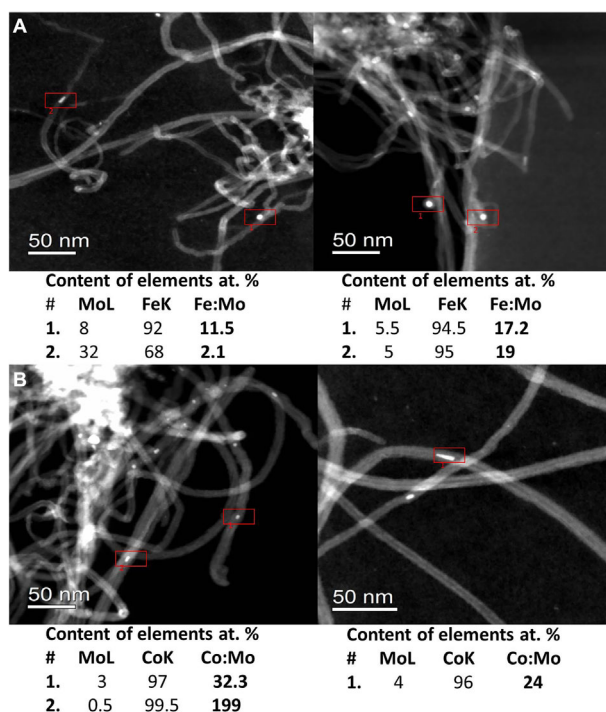


Figure 8. STEM images of MWCNTs and catalytic particles encapsulated within their channels obtained using (A) 40%(Fe₂Mo)/Al₂O₃ and (B) 40%(Co₂Mo)/Al₂O₃ catalysts and EDS data on the chemical composition of particles under study.

Fe and Co. Thus, STEM and EDS data on the composition of catalyst particles encapsulated within nanotube channels indicate that in the case of Fe–Mo catalysts the Mo atoms are the constituents of active particles (up to 30 at.%), while in the

case of Co–Mo catalyst the Mo content in active particles does not exceed 3–4 at.% (see **Figure 8**).

The decrease in the yield of MWCNTs with increasing content of the active component up to 70 wt.% can be attributed to the formation of larger metal particles due to the easier sintering of these catalysts. The average outer diameter of MWCNTs is different for the Fe–Mo and Co–Mo catalysts of varied active component concentration (**Figures 9 and 10**).

Low-resolution TEM images reveal that MWCNTs are capable of a partial self-organization during the growth process, which leads to the formation of agglomerates represented by coils of various sizes (**Figure 9 and 10**). In the case of MWCNTs obtained using Fe–Mo/Al₂O₃ catalysts, their morphology virtually does not change with the catalyst composition. The thinnest MWCNTs with a narrower diameter distribution are formed using the 40% (Fe₂Mo)/Al₂O₃ catalyst. In this case, the nanotubes have the following characteristics: the average outer diameter of 5–10 nm, the inner diameter of 3–5 nm, and the number of walls of 8–13. Varying the Fe/Mo metal ratio in the active component from 2:1 to 16:1 leads to a minor change in the average diameter of the MWCNTs, from 8.4 to 9.8 nm, respectively (**Figure 9B–D**). An increase in the total content of the Fe–Mo active component from 40 to 70 wt.% also does not lead to the significant changes of the average tube diameter that varies from 9.77 to 9.42 nm, respectively. It should be noted that the number of walls (8–13) and the inner diameter (3–5 nm) remain unchanged for different content of the active component and Fe/Mo ratio (**Figure 9D**). According to TEM data for the MWCNT samples obtained using Co–Mo/Al₂O₃ catalysts, the formation of the thinnest tubes is observed for the 30% (Co₁₆Mo)/Al₂O₃ sample. MWCNT characteristics are the following: the average number of walls 6–10 and internal diameter 3–4 nm. MWCNTs obtained using the catalyst with the maximum molybdenum content (40% Co₂Mo/Al₂O₃) have an average diameter of 10.7 nm, a maximum number of walls of 10–16 and internal diameter of 2–3 nm. An increase in the content of the active component from 30 to 60 wt.% (**Figure 10B–D**) does not affect the characteristics of the produced MWCNTs (the average diameter varies from 8.6 to 9.22 nm, the average number of walls is 7–11, and internal diameter is 3–4 nm).

3.3. Influence of the Catalyst Composition on Defectiveness of MWCNTs

Our previous papers demonstrated the high sensitivity of Raman spectroscopy for estimation of the defective structure of MWCNTs and graphene flakes deposited on the nanotube surface.^[54–56] The

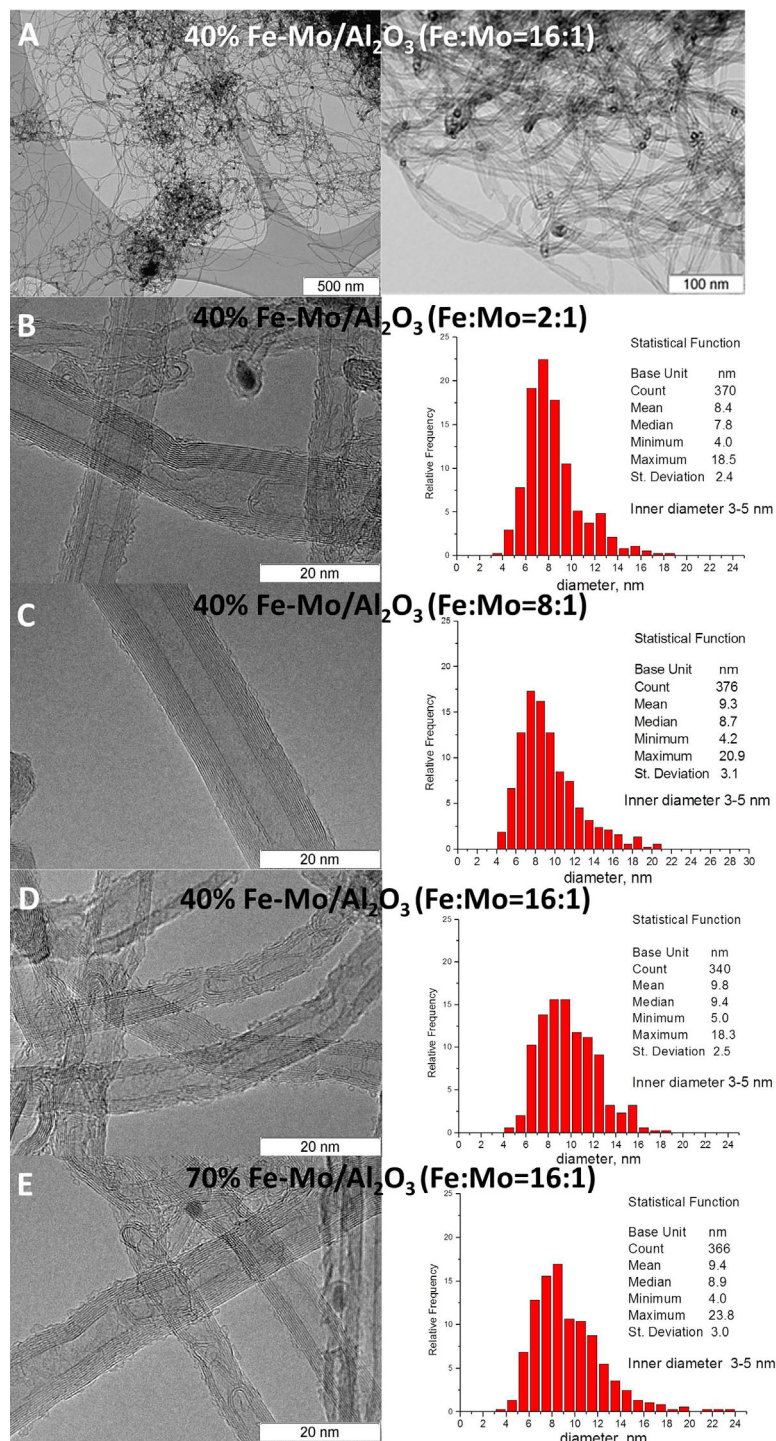


Figure 9. (A) Low- and (B–E) high-resolution TEM images of MWCNT samples obtained using Fe–Mo/Al₂O₃ catalysts with different ratio of the active component metals, Fe/Mo = 2:1, 8:1, 16:1 (B–D), and different content of the active component, 40 and 70 wt.% (D and E), and their diameter distributions.

graphene fragments have been proposed to form a mosaic structure of nanotube walls.^[54]

The intensity ratio of D (induced mode) and G (tangential mode) bands of graphene fragments can be used to estimate the

degree of disorder in the structure of carbon materials. The analysis of 2D behavior (two-phonon scattering) of a strip is mainly used to reveal a number of graphene layers and their mutual orientation (the order of superposition).^[57] **Figure 11**

displays the Raman spectra of MWCNTs produced using Co–Mo catalysts with the variable content and ratio of active metals. The increase in the Mo content increases the intensity of 2D Raman bands, while variations in the intensities of D and G bands are insignificant (**Figure 11B**).

Figure 12 demonstrates the dependence of intensity ratios $I_{2D/D}$ and $I_{D/G}$ on the Co–Mo active component content and Co/Mo molar ratio in the active component. In the case of the 40%(Co₂Mo)/Al₂O₃ catalyst, MWCNTs with a less defective structure are obtained, but this catalyst shows a very low productivity in the MWCNT growth reaction.

An increase in the total content of the active Co–Mo component (with Co/Mo = 16:1) from 30 to 60 wt.% leads to the formation of MWCNTs with a higher degree of defectiveness (**Figure 11** and **12(A)**). In the case of Fe–Mo catalysts, both the increase in the total content of the active component from 40 to 70 wt.% at a Fe/Mo ratio of 16:1 and the increase in the Mo content in the catalyst containing 40 wt.% with a variable Fe/Mo ratio lead to the growth of MWCNTs with a less defective structure (**Figures 13** and **14**).

The temperature dependences of conductivity σ (T) of MWCNTs produced on different types of Fe–Mo and Co–Mo catalysts (linearized in the $\sigma(T)/\sigma_{300K}$ coordinates) are presented in **Figures 15** and **16**. Thus, MWCNTs show a temperature dependence of conductivity as

$$\sigma(T) \sim \exp(-T^{-1/2}),$$

which can be described within the Coulomb blockade theory (the Efros–Shklovskii variable range hopping model^[58] of conductivity) or within the quasi one-dimensional (1-D) variable range hopping conductivity (VRHC) (the Mott law^[59]):

$$\sigma(T) = \sigma_0 \exp\left[(-T_0/T)^{1/2}\right] \quad (1)$$

where σ_0 is constant, $T_0 = C_{VRHC} \alpha^{-1} / k_B N(E_F)$, $C_{VRHC} \approx 1$ for one dimensional VRHC; and $T_0 = T_{ES} = C_{ES} \alpha^{-3} / k_B N(E_F)$, $C_{ES} = (2.8/4\pi)$, α^{-1} is the length by which the amplitude of the wave function falls down ($\alpha^{-1} \approx 10$ Å), $N(E_F)$ is the density of localized states at the Fermi level E_F , and k_B is the Boltzmann constant. Note that both mechanisms of the dependence (Eq. (1)) (one dimensional VRHC or ES) take place in the inversely proportional dependence of $N(E_F)$ on parameter T_0 . $N(E_F)$ can be used to estimate the charge carrier concentrations n from the $n \sim 2/3N(E_F)/E_F$ ratio.^[60]

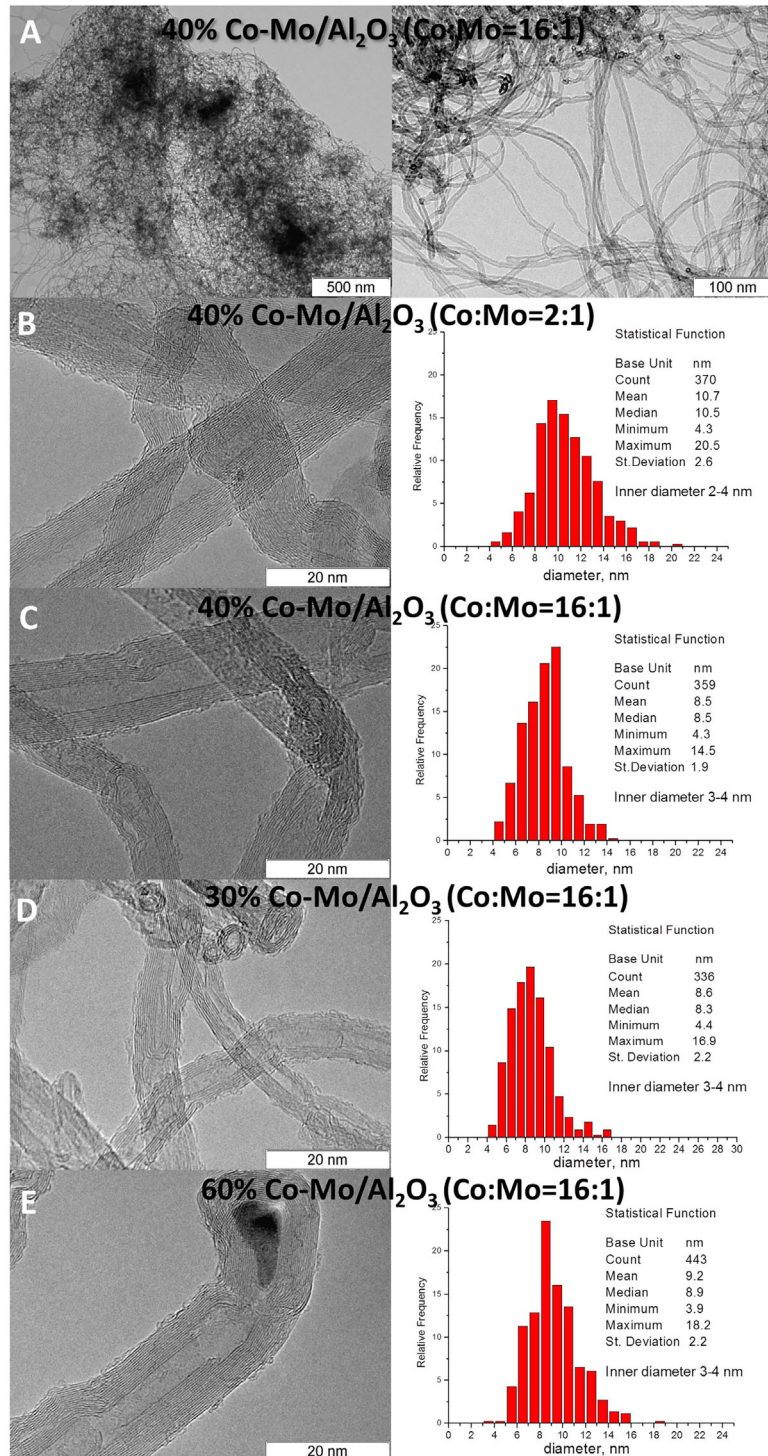


Figure 10. (A) Low- and (B–E) high-resolution TEM images of MWCNT samples obtained using Co–Mo/Al₂O₃ catalysts with different ratio of the active component metals, Co/Mo = 2:1, 8:1, 16:1 (B–D), and different content of the active component: 30, 40, and 60 wt.% (C–E), and their diameter distributions.

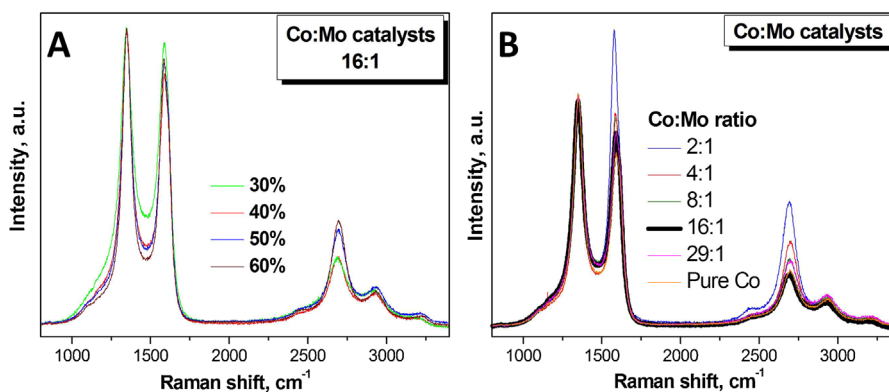


Figure 11. Raman spectra of MWCNTs synthesized using Co–Mo catalysts with the variable content (A) and ratio of active metals (B).

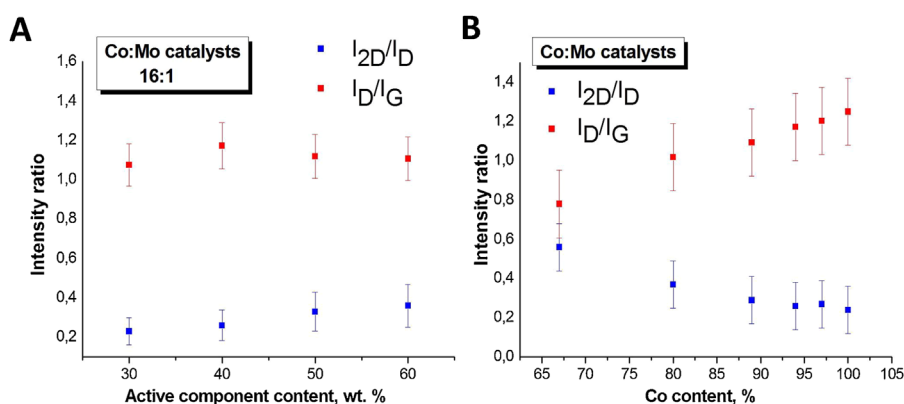


Figure 12. The dependence of intensity ratios I_{2D}/I_D and I_D/I_G on the Co–Mo active component content (A) and Co/Mo molar ratio in the active component (B).

Thus, data shown in **Figures 17 and 18** allow the concentration of current carriers in the MWCNTs to be estimated. The decrease in the Fe content in Fe–Mo catalysts increases the concentration of current carriers, thus indicating the decreasing concentration of defects in MWCNTs. These results correlate with the Raman spectroscopy data (Figure 14). The I_{2D}/I_D ratio increases with the Fe content in the catalyst, which also points to the reduction in the number

of defects. The opposite effect is observed for the Co–Mo catalysts. An increase in the Co content in Co–Mo samples leads to MWCNTs with the highest concentration of current carriers, which also indicates a decrease in MWCNT defectiveness. These results are consistent with the Raman data. The I_{2D}/I_D ratio increases with increasing the Co content in the catalyst, which corresponds to an increase of the graphene block size in nanotube walls.

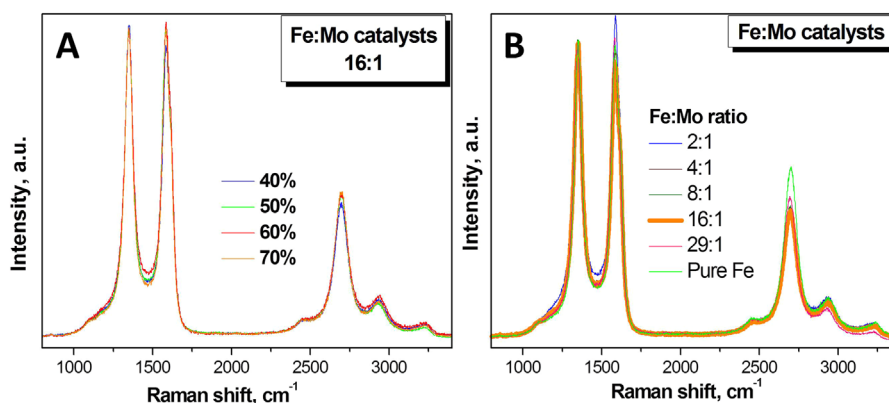


Figure 13. Raman spectra of MWCNTs synthesized using Fe–Mo catalysts with the variable content (A) and ratio of active metals (B).

and b) the active component content from 30 to 70 wt.% at a fixed metal ratio (16:1).

1. Data on the formation of active bimetallic alloy particles were obtained by in situ XRD, ex situ XPS, and STEM&EDS. It was found that despite the formal similarities of Fe–Mo and Co–Mo catalysts, their activation in the reaction mixture (C_2H_4 –Ar) results in the formation of alloys with very different Mo atomic content. In the case of Fe-containing catalysts, the major part of Mo is incorporated into the active component, in contrast to Co-based catalysts. The stable carbide formation for such systems is not observed. The absence of stable carbides promotes effective diffusion of carbon through the metal particle, thus, ensuring a much higher activity of multicomponent Fe–Mo catalysts as compared to the activity of monometallic Fe catalyst.
2. The addition of small quantities of Mo to the Fe-based catalysts enhances their activity in the MWCNT growth. 40% (Fe₁₆Mo)/Al₂O₃ was found to be the most active sample. An increase in the content of the active component from 40 to 70 wt.% at a Fe/Mo ratio of 16:1 decreases the activity of the Fe–Mo catalyst in the MWCNT growth process.
3. The addition of Mo to the Co-containing catalyst does not increase its activity in the MWCNT growth reaction. Most active is the sample containing monometallic Co. An increase in the content of the active component from 30 to 60 wt.% at a Co/Mo ratio of 16:1 decreases the activity of the Co–Mo catalyst in the MWCNT growth reaction.
4. The defectiveness of the MWCNTs produced using Fe–Mo and Co–Mo catalysts with a variable composition was estimated by Raman spectroscopy in combination with measurements of the temperature dependence of nanotube conductivity. Thus, in the case of Fe–Mo catalysts, the current carrier concentration in MWCNTs slightly increases with increasing the Mo content. For the Co–Mo catalysts, a decrease in the current carrier concentration in nanotubes produced using the catalyst with a higher Mo content is observed. For the Fe-containing catalysts, the addition of Mo and an increase of the active component concentration from 40 to 70 wt.% boost the defectiveness of MWCNTs as compared to the monometallic Fe catalyst. However, the addition of Mo to the Co–Mo catalyst composition significantly reduces the degree of MWCNT defectiveness, especially when 40%(Co₂Mo)/Al₂O₃ is used as a catalyst.

Acknowledgments

The reported study was funded by the Russian Foundation for Basic Research via grants 16-32-60046 mol_a_dk (to M.A. Kazakova to obtain the catalyst samples and MWCNTs) and 15-32-70013 mol_a_mos (to S.N. Bokova-Sirosh to conduct Raman spectroscopic studies).

Conflict of Interest

The authors declare no conflict of interest.

Keywords

defective structure, Fe–Mo and Co–Mo bimetallic catalyst, multi-walled carbon nanotubes, Pechini method

Received: May 31, 2017
Revised: September 18, 2017
Published online: October 27, 2017

- [1] M. F. L. De Volder, S. H. Tawfick, R. H. Baughman, A. J. Hart, *Science* **2013**, 339, 535.
- [2] M. S. Dresselhaus, G. Dresselhaus (Eds.), *Carbon Nanotubes: Synthesis, Structure, Properties, and Applications: Topics in Applied Physics*, Springer-Verlag, Berlin **2001**, ISBN 3-54041-086-4.
- [3] M. Zhang, S. Fang, A. A. Zakhidov, S. B. Lee, A. E. Aliev, C. D. Williams, K. R. Atkinson, R. H. Baughman, *Science* **2005**, 309, 1215.
- [4] G. Lalwani, A. Kwaczala, K. Trinward, P. Shruti, C. Sunny, S. Judex, B. Sitharaman, *Carbon* **2013**, 53, 90.
- [5] Z. Li, V. P. Kunets, V. Saini, Y. Xu, E. Dervishi, G. J. Salamo, A. R. Biris, A. S. Biris, *ACS Nano* **2009**, 3, 1407.
- [6] S. H. Barghi, T. T. Tsotsis, M. Sahimi, *Int. J. Hydrogen Energy* **2014**, 39, 1390.
- [7] I. T. Kim, G. A. Nunnery, K. Jacob, J. Schwartz, X. Liu, R. Tannenbaum, *J. Phys. Chem. C* **2010**, 114, 6944.
- [8] Y. Wei, Y. X. Lin, K. Jiang, P. Liu, Q. Li, S. Fan, *Nano Lett.* **2013**, 13, 4795.
- [9] C. W. Tan, K. H. Tan, Y. T. Ong, A. R. Mohamed, S. H. S. Zein, S. H. Tan, *Environ. Chem. Lett.* **2012**, 10, 265.
- [10] P. Verma, P. Saini, R. S. Malik, V. Choudhary, *Carbon* **2015**, 89, 308.
- [11] Y. Cheng, C. Xu, L. Jia, J. D. Gale, L. Zhang, C. Liu, P. K. Shen, S. P. Jiang, *Appl. Catal. B* **2015**, 163, 96.
- [12] M. Alsawat, T. Altalhi, T. Kumeria, A. Santos, D. Losic, *Carbon* **2015**, 93, 681.
- [13] G. M. Mikheev, V. L. Kuznetsov, K. G. Mikheev, T. N. Mogileva, M. A. Shuvaeva, S. I. Moseenkov, *Tech. Phys. Lett.* **2013**, 39, 337.
- [14] V. L. Kuznetsov, V. I. Suslyayev, I. O. Dorofeev, M. A. Kazakova, S. I. Moseenkov, T. E. Smirnova, D. V. Krasnikov, *Phys. Status Solidi B* **2015**, 252, 2519.
- [15] D. V. Krasnikov, I. O. Dorofeev, T. E. Smirnova, V. I. Suslyayev, M. A. Kazakova, S. I. Moseenkov, V. L. Kuznetsov, *Phys. Status Solidi B* **2018**, 255, 1700256 (this issue).
- [16] I. I. Ovchinnikov, M. A. Shuvaeva, V. L. Kuznetsov, A. S. Lisitsyn, *Adv. Mater. Res.* **2014**, 1040, 399.
- [17] F. Hamidi Malayeri, M. R. Sohrabi, H. Ghourchian, *Int. J. Nanosci. Nanotechnol.* **2012**, 8, 79.
- [18] M. Kolangikhah, M. Maghrebi, K. Ghazvini, N. Farhadian, *Int. J. Nanosci. Nanotechnol.* **2012**, 8, 3.
- [19] J. Robertson, *Mater. Today* **2004**, 7, 46.
- [20] P. J. F. Harris, *Int. Mater. Rev.* **2004**, 49, 31.
- [21] H. Qian, E. S. Greenhalgh, M. S. P. Shaffer, A. Bismarck, *J. Mater. Chem.* **2010**, 20, 4751.
- [22] J. Zhu, H. Peng, F. Rodriguez-Macias, J. L. Margrave, N. Khabashesku, A. M. Imam, K. Lozano, E. V. Barrera, *Adv. Funct. Mater.* **2004**, 14, 643.
- [23] J. Chen, H. Liu, W. A. Weimer, M. D. Halls, D. H. Waldeck, G. C. Walker, *J. Am. Chem. Soc.* **2002**, 124, 9034.
- [24] M. Baibarac, P. Gomez-Romero, *J. Nanosci. Nanotechnol.* **2006**, 6, 289.
- [25] A. S. Andreev, M. A. Kazakova, A. V. Ishchenko, A. G. Selyutin, O. B. Lapina, V. L. Kuznetsov, J.-B. d'Espinose de Lacaillerie, *Carbon* **2017**, 114, 39.
- [26] M. A. Kazakova, V. L. Kuznetsov, N. V. Semikolenova, S. I. Moseenkov, D. V. Krasnikov, M. A. Matsko, A. V. Ishchenko,

- V. A. Zakharov, A. I. Romanenko, O. B. Anikeeva, E. N. Tkachev, V. I. Suslyayev, V. A. Zhuravlev, K. V. Dorozkin, *Phys. Status Solidi B* **2014**, 251, 2437.
- [27] S. I. Moseenkov, D. V. Krasnikov, M. A. Kazakova, V. L. Kuznetsov, A. N. Serkova, *Russ. J. Appl. Chem.* **2016**, 89, 1969.
- [28] F. Danafar, A. Fakhru'l-Razi, M. A. M. Salleh, D. R. A. Biak, *Chem. Eng. J.* **2009**, 155, 37.
- [29] J. Liu, S. Fan, H. Dai, *MRS Bull.* **2004**, 29, 244.
- [30] J.-P. Tessonier, D. Rosenthal, T. W. Hansen, C. Hess, M. E. Schuster, R. Blume, F. Girgsdies, N. Pfander, O. Timpe, D. S. Su, R. Schlogl, *Carbon* **2009**, 47, 1779.
- [31] Q. Zhang, J.-Q. Huang, M.-Q. Zhao, W.-Z. Qian, F. Wei, *ChemSusChem* **2011**, 4, 864.
- [32] M. Kumar, Y. Ando, *J. Nanosci. Nanotechnol.* **2010**, 10, 3739.
- [33] A. Fonseca, K. Hernadi, J. B. Nagy, D. Bernaerts, A. A. Lucas, *J. Mol. Catal. A: Chem.* **1996**, 107, 159.
- [34] C. Klinke, J.-M. Bonard, K. Kern, *Surf. Sci.* **2001**, 492, 195.
- [35] H. Kathyayini, N. Nagaraju, A. Fonseca, J. Nagy, *J. Mol. Catal. A: Chem.* **2004**, 223, 129.
- [36] M. Pudukudy, Z. Yaakob, Z. S. Akmal, *Appl. Surf. Sci.* **2015**, 330, 418.
- [37] E. Lobiak, E. Shlyakhova, L. Bulusheva, P. Plyusnin, Y. V. Shubin, A. Okotrub, *J. Alloys Compd.* **2015**, 621, 351.
- [38] S. Mortazavi, A. Reyhani, *Appl. Surf. Sci.* **2008**, 254, 6416.
- [39] P. Landois, A. Peigney, C. Laurent, L. Frin, L. Datas, E. Flahaut, *Carbon* **2009**, 47, 789.
- [40] W.-M. Yeoh, K.-Y. Lee, S.-P. Chai, K.-T. Lee, A. R. Mohamed, *J. Alloys Compd.* **2010**, 493, 539.
- [41] X. Xu, S. Huang, Z. Yang, C. Zou, J. Jiang, Z. Shang, *Mater. Chem. Phys.* **2011**, 127, 379.
- [42] Q. Zhang, Y. Liu, L. Hu, W. Qian, G. Luo, F. Wei, *New Carbon Mater.* **2008**, 23, 319.
- [43] S.-P. Chai, S. H. S. Zein, A. R. Mohamed, *Carbon* **2007**, 45, 1535.
- [44] D. Torres, J. L. Pinilla, M. J. Lázaro, R. Moliner, I. Suelves, *Int. J. Hydrogen Energy* **2014**, 39, 3698.
- [45] V. V. Chesnokov, V. I. Zaikovskii, A. S. Chichkan, R. A. Buyanov, *Appl. Catal. A: General* **2009**, 363, 86.
- [46] M. Popa, J. Frantti, M. Kakihana, *Solid State Ion.* **2002**, 437, 154.
- [47] A. N. Usoltseva, V. L. Kuznetsov, N. A. Rudina, E. M. Moroz, M. Haluska, S. Roth, *Phys. Status Solidi B* **2007**, 244, 3920.
- [48] V. L. Kuznetsov, A. N. Usoltseva, Patent RU2373995 (November 27, **2009**).
- [49] <http://xpspeak.software.informer.com/4.1/>.
- [50] J. H. Scofield, *J. Electron Spectrosc. Relat. Phenom.* **1976**, 8, 129.
- [51] A. I. Romanenko, A. V. Okotrub, V. L. Kuznetsov, A. S. Kotosonov, A. N. Obrastsov, *Phys. Usp.* **2005**, 48, 958.
- [52] A. I. Romanenko, O. B. Anikeeva, V. L. Kuznetsov, T. I. Buryakov, E. N. Tkachev, A. N. Usoltseva, *Sens. Actuators A: Phys.* **2007**, 138, 350.
- [53] V. L. Kuznetsov, D. V. Krasnikov, A. N. Schmakov, K. V. Elumeeva, *Phys. Status Solidi B* **2012**, 249, 2390.
- [54] V. L. Kuznetsov, S. N. Bokova-Sirosh, S. I. Moseenkov, A. V. Ishchenko, D. V. Krasnikov, M. A. Kazakova, A. I. Romanenko, E. N. Tkachev, E. D. Obrastsova, *Phys. Status Solidi B* **2014**, 251, 2444.
- [55] S. N. Bokova-Sirosh, V. L. Kuznetsov, A. I. Romanenko, M. A. Kazakova, D. V. Krasnikov, E. N. Tkachev, Y. I. Yuzyuk, E. D. Obrastsova, *J. Nanophoton.* **2016**, 10, 012526.
- [56] V. L. Kuznetsov, K. V. Elumeeva, A. V. Ishchenko, N. Yu. Beylina, A. A. Stepashkin, S. I. Moseenkov, L. M. Plyasova, I. Yu. Molina, A. I. Romanenko, O. B. Anikeeva, E. N. Tkachev, *Phys. Status Solidi B* **2010**, 247, 2695.
- [57] R. Saito, M. Hofmann, G. Dresselhaus, A. Jorio, M. S. Dresselhaus, *Adv. Phys.* **2011**, 60, 413.
- [58] B. I. Shklovskii, A. L. Efros, *Electronic Properties of Doped Semiconductors*, Springer-Verlag, Berlin **1984**, ISBN 3-540-12995-2.
- [59] N. F. Mott, *Philos. Mag.* **1969**, 19, 835.
- [60] A. A. Abrikosov, *Fundamentals of the Theory of Metals*, North-Holland, Amsterdam **1988**, p. 621.